Potential barrier modification and interface states formation in metal-oxide-metal tunnel junctions

Hyuntae Jung,[1] Yongmin Kim,[1] Kyooho Jung,[1] Hyunsik Im,[1,2,*] Yu. A. Pashkin,[2,3,†] O. Astafiev,[2,3] Y. Nakamura,[2,3] Hosik Lee,[2,3,‡] Y. Miyamoto,[2,3] and J. S. Tsai[2,3]

[1]*Department of Semiconductor Science, Dongguk University, 3-26 Chung-Ku, Pil-Dong, Seoul 100-715, Korea*
[2]*NEC Nano Electronics Research Laboratories and RIKEN Advanced Science Institute, 34 Miyukigaoka, Tsukuba, Ibaraki 305-8501, Japan*
[3]*CREST, Japan Science and Technology Agency, 4-1-8 Honcho, Kawaguchi, Saitama 332-0012, Japan*

(Received 2 April 2009; revised manuscript received 13 July 2009; published 16 September 2009)

We show that the barrier profile of *in situ* grown AlO_x tunnel barriers strongly depends on the material choices of the oxide-metal interface. By doing transport measurements on Al and Nb-based metal-oxide-metal tunnel junctions in a wide temperature range and using the phenomenological Simmons' model, we obtain barrier parameters that are qualitatively consistent with the values obtained from the first-principles calculations. The latter suggest that the formation of metal-induced gap states originating from the hybridization between the metallic bands and Al_2O_3 conduction band is responsible for the tunnel barrier modification. These findings are important for nanoelectronic devices containing tunnel junctions with a thin insulating layer.

DOI: 10.1103/PhysRevB.80.125413 PACS number(s): 73.40.Gk, 73.40.Rw, 73.20.At

I. INTRODUCTION

A thin oxide layer formed in between two metals or semiconductors is a crucial part of a tunnel junction used in various electronic devices.[1,2] Recently, as electronic components scale down and tunnel barrier layers get thinner, requirements for high-quality ultrathin insulating layers become more stringent due to their crucial role in conduction. For a given tunnel structure, the tunnel barrier height depends strongly not only on material properties of the electrodes and the oxide layer but also on the interfaces formed between the insulating layer and electrodes.

In the conventional phenomenological tunnel barrier picture,[3] the tunnel barrier for similar electrodes is represented by a rectangle of width w and height ϕ. The barrier height is approximated by the difference between the work function W of the electrode material and the electron affinity χ of the wide band-gap material forming the tunnel barrier, $\phi = W - \chi$. In this picture, the potential barrier is the region in the energy gap where the electronic density of states vanishes, and the barrier shape is defined at the left and right metal/oxide interfaces by the metallic densities of states of the electrodes and on the top by the density of states in the conduction band of the barrier material. Therefore, there is a close relation between the barrier shape and the electronic density of states. Additional electronic states can be formed at the interfaces between the electrodes and the oxide layer or even within the insulator gap due to, e.g., defects, such as vacancies or impurities. In general, however, extra states may exist even in the structures with a perfect atomic configuration (single crystals). Such states are often referred to as "metal-induced gap states (MIGS)" that were first introduced for a metal-semiconductor interface,[4] and may be responsible for the lower potential barrier height ϕ than what follows from the phenomenological model. For example, recent work on the Si/SiO_2 system with an ultra thin SiO_2 tunnel barrier proves the existence of the fundamental limit on the barrier thickness due to the *intrinsic* interface region having electronic properties different from the properties of the barrier insulator.[5]

Recently, the concept of the MIGSs has been further extended to explain the tunnel barrier height at various tunnel junction interfaces including interface between perovskite oxides,[6] metal-organic interface,[7] and hybrid organic-inorganic interface.[8] However, in metal/thin oxide/metal tunnel junctions where spatial extent ξ of the interface states into the oxide may become comparable with the thickness of the barrier oxide w, although the importance of the metal/oxide interface was recognized,[9] very little attention was paid to the effects of the interface on transport, and experimental investigation supported by the calculations based on the interface electronic-band theory has not been reported.

In this work, we study *all in situ grown* metal-oxide-metal tunnel junctions consisting of Al bottom electrode, AlO_x tunnel barrier and a top electrode made of either Al or Nb, two superconductors commonly used in the Josephson junction integrated circuits[10] and qubits.[11] Although it is now well recognized that MIGSs formed at various interfaces modify the tunnel barrier height, no comparison of the barrier parameters obtained from the transport measurements and first-principles calculations was done for metal-oxide-metal tunnel junctions. We explore, both experimentally and theoretically, how the microscopic variations in the electronic densities of states at the tunnel junction interface affect the tunnel barrier properties. Besides using two different metals as top electrodes, we also deposit a thin interfacial layer of Al or Nb between the tunnel barrier and the top electrode in some junctions keeping other structural parameters unchanged.

We observed a striking difference in the transport properties of tunnel junctions having different interface compositions. Using a phenomenological Simmons' model we estimated the barrier height for various types of tunnel junctions. The difference in barrier heights suggests the formation of metal-induced gap states in the interface region, which is confirmed by the first-principles calculations. MIGS at the

 ©2009 The American Physical Society

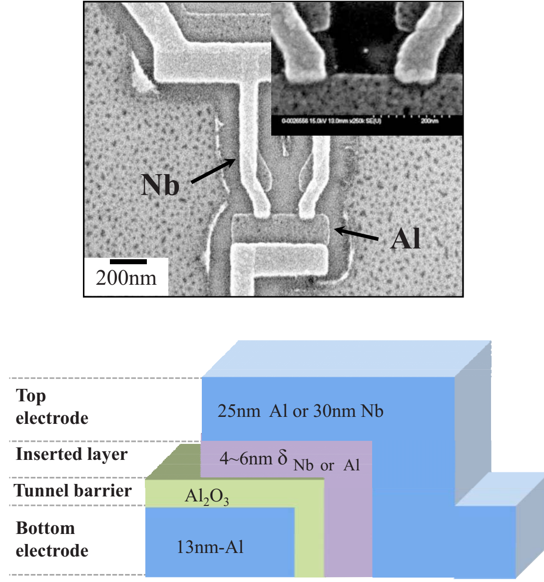

FIG. 1. (Color online) (Top) Scanning electron micrograph of an $Al/AlO_x/Nb$ tunnel junction. The inset shows the magnified view of the junctions. (Bottom) Schematic diagram of the tunnel junction cross-section.

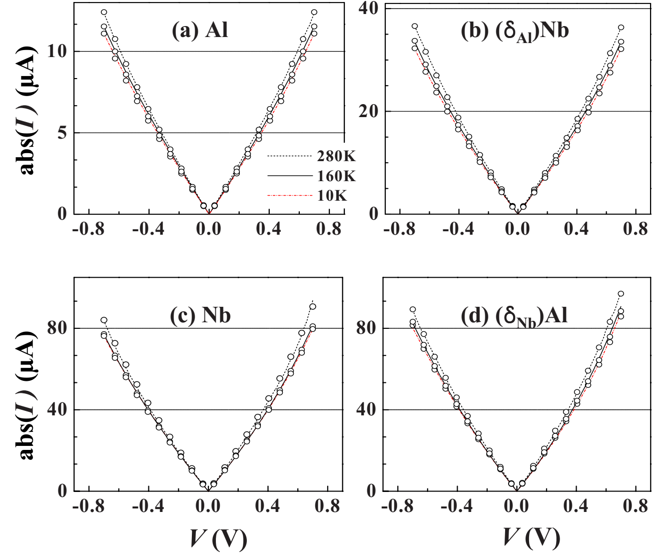

FIG. 2. (Color online) Temperature dependence of the *I-V* characteristics for all measured samples. The legends on the plots indicate the top electrode. The circles and lines represent the measured and fitted data, respectively.

AlO_x/Nb interface have a lower energy and their metallic wave-function penetrates more into the AlO_x layer compared with those at the AlO_x/Al interface. The fitted barrier height values are qualitatively consistent with those obtained from the first-principles calculations.

II. DEVICE FABRICATION

Our tunnel junctions (see Fig. 1) are fabricated by a conventional two-angle deposition technique using a suspended Ge mask formed by electron-beam lithography and supported by a thermally stable polymer phenylene-ether-sulfone (PES).[12] The bottom layer is always a 13 nm thick Al, and the *in situ* tunnel barrier is created by thermal oxidation of the bottom layer at a pressure of 0.1 mbar for 20 min. The tunnel junction is then completed by depositing an interfacial layer and the top electrode. Four types of tunnel junctions were measured: $Al/AlO_x/Al$, $Al/AlO_x/(\delta_{Al})Nb$, $Al/AlO_x/Nb$, and $Al/AlO_x/(\delta_{Nb})Al$. Thus, all our junctions have two interfaces: Al/AlO_x bottom interface and either AlO_x/Al or AlO_x/Nb top interface. The types of tunnel junctions are marked on the corresponding plots. The thicknesses of the top Al and Nb are 25 nm and 35 nm, respectively. δ_{Al} and δ_{Nb} are the interfacial layers, typically 4 or 6 nm thick. The total junction area, as estimated from the SEM image, is $\sim 5,000\ nm^2$. Although each device consists of two tunnel junctions in parallel, we assumed as if it would be a single junction.

III. TRANSPORT MEASUREMENTS AND MODELING

A. Current-voltage (I-V) characteristics

First, we measure the junctions' current-voltage (*I-V*) characteristics at various temperatures and plot them in Fig. 2 as solid lines. Let us note that the main transport mechanism is the electron tunneling and the contribution from the thermionic emission for the bias voltage up to ± 0.7 V is a few orders of magnitude smaller. Higher bias voltage usually results in junction's breakdown. The *I-V* curves of the samples with the AlO_x/Al top interface [Fig. 2(a) and 2(b)] remain symmetric at all temperatures having a difference of less than 0.5% between the currents at +0.7 V and −0.7 V at 280 K. On the contrary, the junctions with the AlO_x/Nb top interface [Fig. 2(c) and 2(d)] have a clear asymmetry between the positive and negative branches with a difference in currents reaching 11%. One more observation is that the junction tunneling resistance of the samples with the AlO_x/Al top interface is always higher as compared to the resistance of junctions with AlO_x/Nb interface. The observed interface-dependent *I-V* characteristics indicate that the barrier height is determined not only by the bulk properties of a metal or tunnel oxide but by the nature of the oxide/metal interface region.

B. Simmons' tunneling current model

We model the measured *I-V* characteristics for all types of junctions denoting the barrier height of the trapezoidal potential at the AlO_x/Al and AlO_x/Nb interfaces as ϕ_0 and ϕ_1, and using them as well as w and dielectric constant of the oxide as fitting parameters. The modeled *I-V* characteristics are plotted as open circles in Fig. 2. Below is the description of the modeling procedure.

The current density $J(V)$ of a tunnel junction at a finite temperature T can be written as[13]

$$J(V) = \frac{4\pi m^* e k_B T}{h^3} \int_0^{E_m} T(E) \times \ln\left\{\frac{1+\exp[(E_F - E)/k_B T]}{1+\exp[(E_F - E - eV)/k_B T]}\right\} dE, \quad (1)$$

where $T(E)$ represents the tunneling transmission coefficient depending on the incident electron energy E in the emitter metal electrode, and E_m is the maximum potential barrier height at a given bias V, m^* is the effective electron mass, e is the electron charge, k_B and E_F are the Boltzmann constant and Fermi energy, respectively. The image force modifies the barrier such that a rectangle of height ϕ_0 and width w is transformed under the bias voltage V as,[14]

$$\phi(x) = \phi_0 - \frac{eVx}{w} - \lambda \frac{w^2}{x(w-x)}, \quad (2)$$

where $\lambda = 0.795 e^2/16\pi w \varepsilon_0 \varepsilon_r$, ε_r is the dielectric constant, and x is the distance from the bottom electrode within the barrier.

C. Fitting and extraction of the barrier parameters

To extract ϕ_0 and ϕ_1 at the two interfaces, the measured *I-V* characteristics are modeled using Eqs. (1) and (2). Fully numerical calculations using "transfer matrix technique" were performed.[15] In this technique, the image force corrected potential in Eq. (2) is approximated by a series of 1 Å-thick equally spaced constant potential slabs, and $T(E)$ is computed using the boundary conditions that the electron wave function and its derivative are continuous across each interface. The effective electron mass m^* for Al, Nb, and AlO_x is $1.16m_0$, $1.6m_0$, and $0.75m_0$ respectively, where m_0 is the free electron mass.[16] First, we model the measured *I-V* curves of the *symmetric* $Al/AlO_x/Al$ junction, using ϕ_0, w, and ε_r as fitting parameters. An outline of the parameter extraction procedure follows: (i) with a trial value of $\varepsilon_r \sim 5$, which is reasonably close to the expected final value we extract the values of ϕ_0 and w modeling the measured *I-V* curve in the low bias region of ± 30 mV where the effect of the bias voltage on the barrier height is small. (ii) With the extracted values of ϕ_0 and w, the full *I-V* curve up to ± 0.7 V is modeled to obtain a new value of ε_r. (iii) If the modeled *I-V* curve is in a good agreement with the measured one, a set of $\phi_{0,1}$, w, and ε_r is obtained. Otherwise, steps (i) and (ii) are repeated *self-consistently* with a new trial value of ε_r until a good agreement is reached. The criterion by which the good agreement is judged is that $\mathrm{abs}(I_{\mathrm{measured}} - I_{\mathrm{modeled}})/I_{\mathrm{measured}} < 0.03$ at each bias voltage up to 0.7 V. For all temperatures, the same procedure is repeated to have the temperature dependence of the parameters. It turns out that while the extracted values of $\phi_0 \sim 2.2$ eV and $w \sim 1$ nm show negligible temperature dependence, ε_r varies from 5.60 to 5.25 as the temperature increases from 10 to 280 K. The modeled w of ~ 1 nm is consistent with the thickness estimated using high-resolution transmission electron microscopy. Next, since the bottom Al electrode and AlO_x tunnel barrier of all the samples were created under the same fabrication conditions, we use w and ϕ_0 obtained for the symmetric $Al/AlO_x/Al$ junction for modeling the *I-V* characteristics of the other samples having a different top electrode. Thus, for the other devices, ϕ_1 at the top AlO_x/metal interface and ε_r are the parameters used in modeling the measured *I-V* characteristics, and their values are obtained in a similar way.

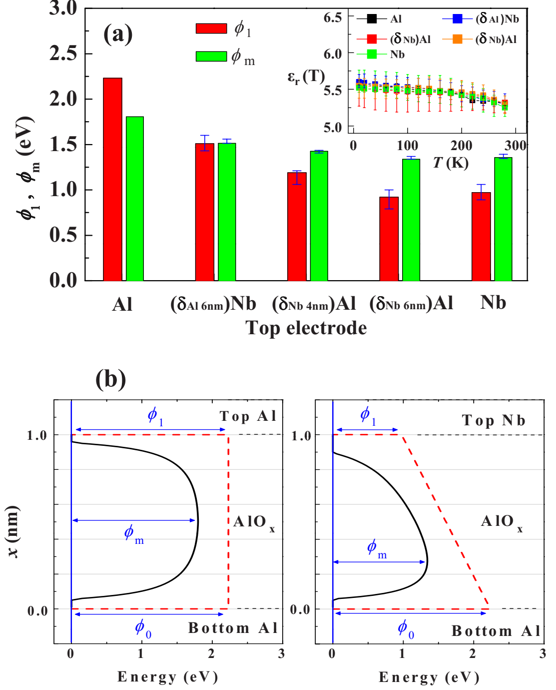

FIG. 3. (Color online) (a) Modeled parameters (ϕ_1, ϕ_m). The inset shows the modeled values of ε_r as a function of temperature. (b) Calculated potential profiles for the $Al/AlO_x/Al$ and $Al/AlO_x/Nb$ tunnel junctions using the parameters at 280 K.

Figure 3 shows the variation of ϕ_1 with different interface configurations. It is clear that ϕ_1 at the AlO_x/Nb interface (~ 1.0 eV) is significantly smaller than that at the AlO_x/Al interface (~ 2.2 eV). The extracted values of the junction parameters yield a zero-bias maximum potential height (ϕ_m) which electrons actually feel to be 1.75 eV for $Al/AlO_x/Al$ and 1.25 eV for $Al/AlO_x/Nb$ tunnel junctions. The extracted values of barrier height are reasonably comparable with reported values for various AlO_x/metal junction devices with different thicknesses of AlO_x layer.[17]

The error for each data point is calculated as follows. We just assumed that the electron mass m^* in the emitter electrode and AlO_x layer as well as the junction areas have uncertainties of $\pm 20\%$ and $\pm 10\%$, respectively. These uncertainties result in errors of ϕ_1 shown as error bars in Fig. 3(a).

The inset of Fig. 3 shows the temperature dependence of ε_r for the AlO_x tunnel barrier. Since all the barriers were created under the same conditions, one can expect that the temperature dependence of ε_r should be similar for all types of junctions. This is what we actually obtain from modeling the transport characteristics [see inset of Fig. 3(a)]. However, comparison of the obtained ε_r with the values reported in the literature is not straightforward. The reported values for ε_r scatter between 3.4 and 11.5 depending, probably, on the fabrication conditions.[18] We just note that our values do not contradict the reported ones.

Figure 3(b) shows the calculated potential profiles for the $Al/AlO_x/Al$ and $Al/AlO_x/Nb$ tunnel junctions, using the extracted parameters at 280 K. The solid and dashed lines represent the barrier profiles with and without the image force correction, respectively. The fitted value of the barrier height at the $AlO_x/(\delta_{Al})Nb$ $[AlO_x/(\delta_{Nb})Al]$ interface is smaller (larger) than that at the AlO_x/Al (AlO_x/Nb) interface. This is presumably because the inserted Al (Nb) layer is not thick enough to cover the AlO_x surface leading to a mixed interface of AlO_x/Al and AlO_x/Nb. In this case, one can expect that the barrier height is some kind of an average value of ϕ_0 and ϕ_1 depending on the effective area of each interface, as was observed in the experiment.

In the conventional potential barrier picture, since the work function values W for Al and Nb are very close (4.25 eV for Al and 3.99 eV for Nb),[19] one can expect ϕ_0 at the Al/AlO_x interface and ϕ_1 at the Nb/AlO_x interface to be quite similar. However, the experimentally extracted values of ϕ_0 and ϕ_1 using tunneling transport measurements differ by more than 1 eV [see Fig. 3(b)]. In order to understand the interface-dependent barrier height at the microscopic level, we do first-principles calculations and compare electronic band structures of $Al/Al_2O_3/Al$ and $Al/Al_2O_3/Nb$, assuming single crystal Al, Nb, and Al_2O_3.

IV. FIRST-PRINCIPLES CALCULATIONS

In the first-principles calculations, $Al/Al_2O_3/(Al$ or $Nb)$ systems are modeled by a periodically repeated slab that consists of multiple atomic layers, all infinite in the plane of the interface, with the orientation relationship $Al_2O_3(0001)/Nb(Al)(111)$ since it minimizes lattice mismatch.[20] For each stoichiometric slab, metallic electrode parts contain nine Nb layers and six Al layers, and the Al_2O_3 insulating part contains five oxygen and eight Al layers. Adding more atomic layers to Al and Nb electrodes does not change the electronic structure at the interface but makes the calculation time unaffordably long. The first-principles calculations are performed in the scheme of the density-functional theory using the generalized gradient approximation of Perdew *et al.*[21] for the exchange-correlation potential with the plane-wave self-consistent field package.[22] The ultrasoft pseudopotentials with a plane-wave basis set of cutoff energy of 60 Ry are employed.[23] To mimic an isolated $metal/Al_2O_3/metal$ junction, a supercell technique[24] with a 10 Å vacuum space is used while preserving an in-plane periodicity perpendicular to the direction of tunneling with fixed lateral lattice vectors. The Brillouin zone integration is performed within (5 5 1) Monkhorst-Pack grid.[25] The calculations are done assuming Al_2-terminated Al_2O_3/Al interface and Al_3-terminated Al_2O_3/Nb interface, respectively.[26] According to the transmission electron microscopy observations, atomic configuration at the Al_2O_3/Nb interface does not agree with Al-terminated or Al_2-terminated Al_2O_3/Nb interface.[20] Also, the atomic density of Al atoms at the Al_2O_3/Nb interface is 1.5 times larger than that of Al_2O_3, implying an Al_3-terminated Al_2O_3/Nb interface.[27]

The layer-projected partial densities of states (PDOS) of Al atoms along the transport direction (x axis) are displayed

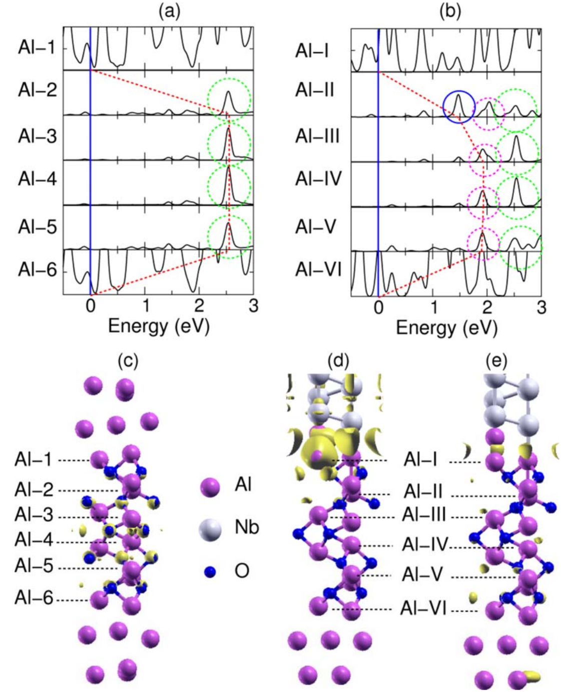

FIG. 4. (Color online) (a)–(b) The layer-projected partial density-of-states (PDOS) of Al atoms along the transport direction (x axis) for $Al/Al_2O_3/Al$ and $Al/Al_2O_3/Nb$ systems. The blue vertical lines represent the Fermi level. The red lines show the PDOS profiles obtained by connecting the main large peaks' positions. The encircled peaks are discussed in the text. (c) The relaxed atomic structures of the $Al/Al_2O_3/Nb$ tunnel junction with the charge density of the Al_2O_3 conduction band corresponding to the PDOS peaks marked by the green circles in Fig. 4(a). (d)–(e) The relaxed atomic structures of the $Al/Al_2O_3/Nb$ tunnel junction with the charge densities of the MIGS marked by dotted blue and dashed magenta in Fig. 4(b).

in Figs. 4(a) and 4(b) for $Al/Al_2O_3/Al$ and $Al/Al_2O_3/Nb$ systems, respectively. Each graph contains a number of peaks corresponding to a particular Al layer inside Al_2O_3. The Al layers are marked by the Arabic numerals in $Al/Al_2O_3/Al$ system [Fig. 4(a)] and Roman numerals in $Al/Al_2O_3/Nb$ system [Fig. 4(b)]. Similar numeration is used in Figs. 4(c)–4(e).

V. DISCUSSION

We obtain PDOS profiles for both systems by connecting the large peaks' positions [dashed red lines in Figs. 4(a) and 4(b)]. At the Al top and bottom layers (1 and 6 in the $Al/Al_2O_3/Al$ system and I and VI in the $Al/Al_2O_3/Nb$ system), the ends of the red line are set to zero, which corresponds to the Fermi level. Although they are not exactly the same, the PDOS profiles can be compared, on the qualitative level, with the Simmons' potential barriers shown in Fig. 3(b): the profile is symmetric in the $Al/Al_2O_3/Al$ system and asymmetric in $Al/Al_2O_3/Nb$ one. Also, in the latter system the profile is lower than that in the former one.

The partial densities of states in Figs. 4(a) and 4(b) can be related to the corresponding charge density plots shown in

Figs. 4(c)–4(e). In the $Al/Al_2O_3/Al$ system, a number of peaks located at 2.6 eV and encircled by the green dotted line form the Al_2O_3 conduction band, and the corresponding charge density represented by yellow balloons exists only in Al_2O_3 region, as shown in Fig. 4(c). Similar peaks located at the same energy are also present in the $Al/Al_2O_3/Nb$ system but they do not have any effect on conductance due to the formation of two types of MIGS at lower energies. The first type, encircled by the blue dotted line in Fig. 4(b), has a corresponding charge density shown in Fig. 4(d). These MIGS are interface states that are strongly localized in Al regions and nearby Nb layers. It also penetrates partly into $Al/Al_2O_3/Al$ region as can be seen in Fig. 4(d). The observed asymmetry of the PDOS profile is mainly caused by these MIGS. MIGS of the other type are marked by the magenta circles in Fig. 4(b) with the charge density presented in Fig. 4(e). These are bonding states between the interface states and Al_2O_3 conduction band with a minor contribution from the bulk metallic states. One can see in Fig. 4(e) that the charge density is largest at the Nb/Al_2O_3 interface and in Al_2O_3 region. It is clear that the bonding nature of these MIGS pulls down the peak position of PDOS in energy axis resulting in the lower potential barrier.

There is a qualitative difference between the metal-induced gap states and evanescent metallic states in the band gap region. For the former, the overlap of at least two wave functions is crucial.[28] The latter, however, are formed due to the penetration of a single wave function into the band-gap region. Large overlap leads to the formation of MIGS causing the band gap reduction at the nanoscale. Among the Nb 4d states, $d_{3z^2-r^2}$ orbital component has the largest overlap with interface Al 3s orbital so that its contribution to the two MIGS in Fig. 4(b) is most significant, as shown in Fig. 4(d).

Similar PDOS calculations with Al-terminated or Al_2-terminated Al_2O_3/Nb interfaces show that MIGS are not formed. We note also, that MIGS formed at the Al_3-terminated Al_2O_3/Nb interface with a thicker AlO_x layer may have a lower density of states, so that their effect on the tunnel barrier can be weaker. It also follows from our calculations that the MIGS at the Nb/Al_2O_3 interface penetrate into Al_2O_3 with a penetration depth ξ of ~ 3 Å. Thus, in the $Al/Al_2O_3/Nb$ system with an even thinner Al_2O_3 barrier, this feature may further affect the potential barrier height.

As AlO_x becomes thicker, the magnitude of MIGSs-induced barrier height lowering becomes weak. This is simply because oxide thickness w becomes larger than ξ. Thus, though the same parameter extraction method is used for similar tunnel junction devices having different thickness of AlO_x, effective barrier height of AlO_x can be given differently. As w becomes thicker, extracted effective barrier height is expected to become larger and eventually saturated. This may be one of reasons for the scattered values of extracted barrier height for similar metal/AlO_x tunnel junction devices having MIGSs at the tunnel junction interface.

Although direct comparison of the results obtained from the Simmons' model discussing the potential barrier shape and first-principles calculations of the electronic density of states is not straightforward, however, as we discussed in the introduction, there is a close relation between them. One can see that the latter reproduce correctly, at least at the qualitative level, all the essential differences between $Al/Al_2O_3/Al$ and $Al/Al_2O_3/Nb$ structures that were observed in the transport measurements. The quantitative difference between the two results can be partly attributed to the fact that the calculated single crystal structures are different from the "real" tunnel junctions with polycrystalline electrodes separated by amorphous insulating layers. Nonetheless, even such imperfect junctions show qualitatively similar tendencies in tunnel barrier shape predicted by the first-principle calculations for a perfect crystal structure. Similar first principles calculations for amorphous metal/oxide/metal tunnel junctions would shed more light on the junctions' barrier properties; however, such calculations would require much more computational power, which is unavailable at the moment.

VI. CONCLUSIONS

We have investigated the dependence of the potential barrier profile on the interface type by measuring at various temperatures *I-V* characteristics of Al and Nb-based tunnel junctions with a thermally oxidized AlO_x tunnel barrier. The barrier height is significantly lower at the AlO_x/Nb interface as compared to that at the AlO_x/Al interface. The first-principles calculations suggest that the metal-induced gap states at the AlO_x/Nb interface are responsible for the barrier asymmetry and reduction of the barrier height.

ACKNOWLEDGMENTS

We thank J. P. Pekola for useful comments. H.I. acknowledges the support of the National Research Foundation (NRF) of Korea.

*hyunsik7@dongguk.edu

†On leave from Lebedev Physical Institute, Moscow, Russia; pashkin@frl.cl.nec.co.jp

‡hosiklee@gmail.com

[1] *Single Charge Tunneling: Coulomb Blockade Phenomena in Nanostructures*, edited by H. Grabert and M. H. Devoret (Plenum, New York, 1992).

[2] *Silicon Nanoelectronics*, edited by S. Oda and D. Ferry (CRC Press, Boca Raton, 2005).

[3] *Tunneling Phenomena in Solids*, edited by E. Burnstein and S. Lundqvist (Plenum, New York, 1969).

[4] J. Tersoff, Phys. Rev. Lett. **52**, 465 (1984).

[5] D. A. Muller, T. Sorsch, S. Moccio, F. H. Baumann, K. Evans-Lutterodt, and G. Timp, Nature (London) **399**, 758 (1999).

[6] K. Janicka, J. P. Velev, and E. Y. Tsymbal, Phys. Rev. Lett. **102**, 106803 (2009).

[7] M. G. Helander, Z. B. Wang, J. Qiu, and Z. H. Lu, Appl. Phys. Lett. **93**, 193310 (2008).

[8] K. Y. F. Tsai, M. G. Helander, and Z. H. Lu, J. Appl. Phys. **105**, 083706 (2009).
[9] E. Tan, P. G. Mather, A. C. Perrella, J. C. Read, and R. A. Buhrman, Phys. Rev. B **71**, 161401(R) (2005); T. W. Hickmott, J. Appl. Phys. **89**, 5502 (2001); D. Stoeffler, Europhys. Lett. **59**, 742 (2002); I. I. Oleinik, E. Yu. Tsymbal, and D. G. Pettifor, Phys. Rev. B **62**, 3952 (2000); I. G. Batirev, A. Alavi, M. W. Finnis, and T. Deutsch, Phys. Rev. Lett. **82**, 1510 (1999).
[10] IEICE Trans. Electron. E91-C, (2008).
[11] Quantum Inf. Process. 8, (2009).
[12] R. Dolata, H. Scherer, A. B. Zorin, and J. Niemeyer, J. Vac. Sci. Technol. B **21**, 775 (2003); Hyunsik Im, Yu. A. Pashkin, T. Yamamoto, O. Astafiev, Y. Nakamura, and J.–S. Tsai, *ibid.* **25**, 448 (2007).
[13] J. G. Simmons, J. Appl. Phys. **35**, 2655 (1964).
[14] J. G. Simmons, in *Tunneling Phenomena in Solids*, edited by E. Burstein and S. Lundqvist (Plenum, New York, 1969), p. 135.
[15] R. Tsu and L. Esaki, Appl. Phys. Lett. **22**, 562 (1973).
[16] A. I. Kiselev, L. A. Akashev, and V. I. Kononenko, Tech. Phys. **49**, 302 (2004); M. H. Halloran, J. H. Condon, J. E. Graebner, J. E. Kunzier, and F. S. L. Hsu, Phys. Rev. B **1**, 366 (1970); W. H. Rippard, A. C. Perrella, F. J. Albert, and R. A. Buhrman, Phys. Rev. Lett. **88**, 046805 (2002).
[17] E. Cimpoiasu, S. K. Tolpygo, X. Liu, N. Simonian, J. E. Lukens, K. K. Likharev, R. F. Klie, and Y. Zhu, J. Appl. Phys. **96**, 1088 (2004) and refer to references therein.
[18] *The Electrical Engineering Handbook*, edited by R. C. Dorf, (CRC Press, Boca Raton, 1993); *Electronics Engineers' Handbook*, edited by D. Christiansen, (McGraw-Hill, New York, 1996); J. Robertson, J. Vac. Sci. Technol. B **18**, 1785 (2000).
[19] W. Ashcroft and N. D. Mermin, *Solid State Physics* (Holt, Rinehart and Winston, New York, 1976).
[20] G. Gutekunst, J. Mayer, and M. Ruhle, Philos. Mag. A **75**, 1329 (1997).
[21] J. P. Perdew, K. Burke, and M. Ernzerhof, Phys. Rev. Lett. **77**, 3865 (1996).
[22] See http://www.quantum-espresso.org and http://www.pwscf.org.
[23] D. Vanderbilt, Phys. Rev. B **41**, 7892(R) (1990).
[24] R. M. Martin, *Electronic Structure: Basic Theory and Practical Methods* (Cambridge University Press, Cambridge, 2004), Vol. 1.
[25] H. J. Monkhorst and J. D. Pack, Phys. Rev. B **13**, 5188 (1976).
[26] D. J. Siegel, L. G. Hector, and J. B. Adams, Phys. Rev. B **65**, 085415 (2002); W. Zhang and J. R. Smith, Phys. Rev. Lett. **85**, 3225 (2000).
[27] D. Knauss and W. Mader, Ultramicroscopy **37**, 247 (1991).
[28] L. Thien-Nga and A. T. Paxton, Phys. Rev. B **58**, 13233 (1998).